Materials Horizons

ROYAL SOCIETY OF CHEMISTRY

COMMUNICATION

View Article Online
View Journal | View Issue

Cite this: *Mater. Horiz.*, 2021, 8, 3468

Received 27th August 2021,
Accepted 4th November 2021

DOI: 10.1039/d1mh01385h

rsc.li/materials-horizons

Infinite-layer/perovskite oxide heterostructure-induced high-spin states in $SrCuO_2/SrRuO_3$ bilayer films†

Zhe Li,‡[ab] Xiaobing Chen,‡[ab] Yuansha Chen, *[abc] Qinghua Zhang,[ab] Hui Zhang,[ab] Jine Zhang,[ab] Wenxiao Shi,[ab] Bin He,[d] Jinxing Zhang,[e] Jinghua Song,[ab] Furong Han,[ab] Banggui Liu, [ab] Lin Gu, [ab] Fengxia Hu, [ab] Yunzhong Chen,[ab] Baogen Shen[ab] and Jirong Sun *[abdf]

Heterostructures composed of dissimilar oxides with different properties offer opportunities to develop emergent devices with desired functionalities. A key feature of oxide heterostructures is interface electronics and orbital reconstructions. Here, we combined infinite-layered $SrCuO_2$ and perovskite $SrRuO_3$ into heterostructures. A rare high spin state as large as 3.0 μ_B f.u^{-1} and an increase in Curie temperature by 12 K are achieved in an ultrathin $SrRuO_3$ film capped by a $SrCuO_2$ layer. Atomic-scale lattice imaging shows the uniform CuO_2-plane-to-RuO_5-pyramid connection at the interface, where the regularly arranged RuO_5 pyramids were elongated along the out-of-plane direction. As revealed by theoretical calculations and spectral analysis, these features finally result in an abnormally high spin state of the interfacial Ru ions with highly polarized e_g orbitals. The present work demonstrates that oxygen coordination engineering at the infinite-layer/perovskite oxide interface is a promising approach towards advanced oxide electronics.

New concepts

Heterostructures composed of dissimilar oxides offer opportunities to develop emergent devices with desired functionalities. A key feature of these heterostructures is interface electronics and orbital reconstructions. Distinct from general perovskite/perovskite-type heterostructures, the symmetry-mismatch heterostructures consist of oxides with completely different symmetries and atomic configurations and may lead to a strong reconstruction of interfacial spin, charge and orbitals, causing unforeseen effects. In this paper, we demonstrate the unique interface reconstruction and resulting exotic properties by grouping infinite-layered $SrCuO_2$ and perovskite $SrRuO_3$ into heterostructures. The mismatch of apical oxygen ions at this infinite-layer/perovskite heterointerface leads to well-ordered RuO_5 pyramids with an enhanced saturation magnetization and increased Curie temperature. For such a kind of heterostructure, we obtained a magnetic moment as high as ~3 μ_B per Ru, in sharp contrast to previously reported ~1–1.6 μ_B per Ru for bulk $SrRuO_3$. Such a high spin state for Ru ions (3 μ_B per Ru) has not been reported before for (001)-orientated $SrRuO_3$ films, which implies the occurrence of distinct orbital occupations that are unavailable for the perovskite/perovskite heterostructures. Our work demonstrates the great potential of oxygen coordination engineering in the exploration of emergent phenomena in magnetic complex oxides.

1 Introduction

ABO_3-type complex perovskite oxides exhibit a wide range of correlated electronic behavior, such as colossal magnetoresistance, high-T_C superconductivity, a high degree of spin polarization and effects associated with charge and orbital orderings.[1–6] In particular, the bulk properties of these oxides can be tailored in artificial heterostructures or ultrathin films, offering the possibilities to develop emergent devices with desired functionalities.[7–9] Recently, the 4d transition metal oxide $SrRuO_3$ (SRO) has attracted intensive research interest in oxide magnetoelectric devices due to its fascinating itinerant ferromagnetism with a Curie temperature T_c as high as 160 K.[10,11] The bulk SRO has a $GdFeO_3$-type orthorhombic structure,[12,13] exhibiting a rigid rotation of RuO_6 octahedra. This octahedral distortion can be modified *via* substrate strain or interface engineering, which greatly impacts the electrical and magnetic properties of SRO.[14,15] Surprising features have been discovered by grouping SRO with other perovskite oxides, for example, in the increase of T_c in SRO films by capping with a $SrTiO_3$ (STO) layer,[16]

[a] *Beijing National Laboratory for Condensed Matter Physics and Institute of Physics, Chinese Academy of Sciences, Beijing 100190, China. E-mail: yschen@iphy.ac.cn, jrsun@iphy.ac.cn*
[b] *School of Physical Sciences, University of Chinese Academy of Sciences, Beijing 100049, China*
[c] *Fujian Innovation Academy, Chinese Academy of Sciences, Fuzhou, Fujian 350108, China*
[d] *Spintronics Institute, School of Physics and Technology, University of Jinan, Jinan 250022, China*
[e] *Department of Physics, Beijing Normal University, Beijing 100875, China*
[f] *Songshan Lake Materials Laboratory, Dongguan, Guangdong 523808, People's Republic of China*

† Electronic supplementary information (ESI) available. See DOI: 10.1039/d1mh01385h

‡ These authors contributed equally to this work.

the appearance of magnetic skyrmions in the $SrIrO_3$/SRO superlattice due to symmetry breaking,[17] and the coexistence of 2D metallicity and ferroelectricity in the $BaTiO_3$/SRO superlattice.[18] Generally, the large crystal-field splitting leads to a low-spin state (S = 1) of the Ru^{4+} ions with an electron configuration of t_{2g}^4 ($3\uparrow,1\downarrow$).[15,19] The measured saturation moment (M_s) for stoichiometric SRO usually ranges from 1.0 to 1.6 μ_B per formula unit (f.u.).[20–22] Fascinatingly, a high-spin state of $\sim$2.1 μ_B f.u.$^{-1}$ has been achieved in SRO ultrathin films when grown on an oxygen-deficient STO substrate or capped by an oxygen-deficient STO layer.[23–25] The increase in the oxygen vacancy (V_o) population in SRO and the resulting local RuO_5 pyramids were expected to contribute to the enhancement of M_s. However, a high V_o density is difficult to be obtained in SRO due to the volatile nature of RuO_x at high temperature in a high vacuum atmosphere and, moreover, the RuO_5 pyramids introduced by such defect engineering are distributed randomly in the film.[23,26]

We note that interface engineering on SRO has mainly focused on perovskite/perovskite (ABO_3/SRO) type heterostructures. The interfacial RuO_6 and BO_6 octahedra are connected through apical oxygen ions, showing coordination distortion or tilting. In fact, there are many oxides that have a similar structural framework and topotactic relationship as perovskite oxide but with different atomic/electronic configurations, for example, infinite-layered copper oxide $ACuO_2$ (A = Ca, Sr, and Ba). The $ACuO_2$ oxides with an orthorhombic bulk phase can form a perovskite-like thin film with missing apical oxygen.[27,28] When grouping SRO with such an $ACuO_2$ oxide, the interfacial spin, charge and orbital may undergo a strong reconstruction due to the completely different crystal symmetries and atomic configurations of these two oxides, leading to different interfacial properties from the ABO_3/SRO heterostructure. More importantly, the missing apical oxygen and B–O bonds in the z direction may lead to oxygen pyramid structures at the $ACuO_2$/SRO interface, with a very high density and well-ordered arrangement.

Bulk $SrCuO_2$ (SCO) is a typical infinite-layered oxide, which is non-magnetic and insulating.[29,30] The corresponding thin film, which is easily compared, has similar in-plane lattice constants to those of SRO. It is therefore expected to form a high-quality interface with SRO. As reported, thick SCO films have a planar (P)-type oxygen-coordination structure that can be regarded as a sequence of positively charged Sr^{2+} and negatively charged CuO_2^{2-} planes that are alternately stacked along the out-of-plane z direction.[28–30] Upon reducing the film thickness, the P-type structure transforms to a chain (C)-type structure to resolve the polar electrostatic instability.[29,30,34]

In this work, we combined the infinite-layered SCO and perovskite SRO into a symmetry-mismatched heterostructure as shown in Fig. 1(a). A rare high-spin state as large as 3.0 μ_B per f.u. was achieved in ultrathin SRO film capped by an SCO layer. The atomic-scale lattice images revealed the

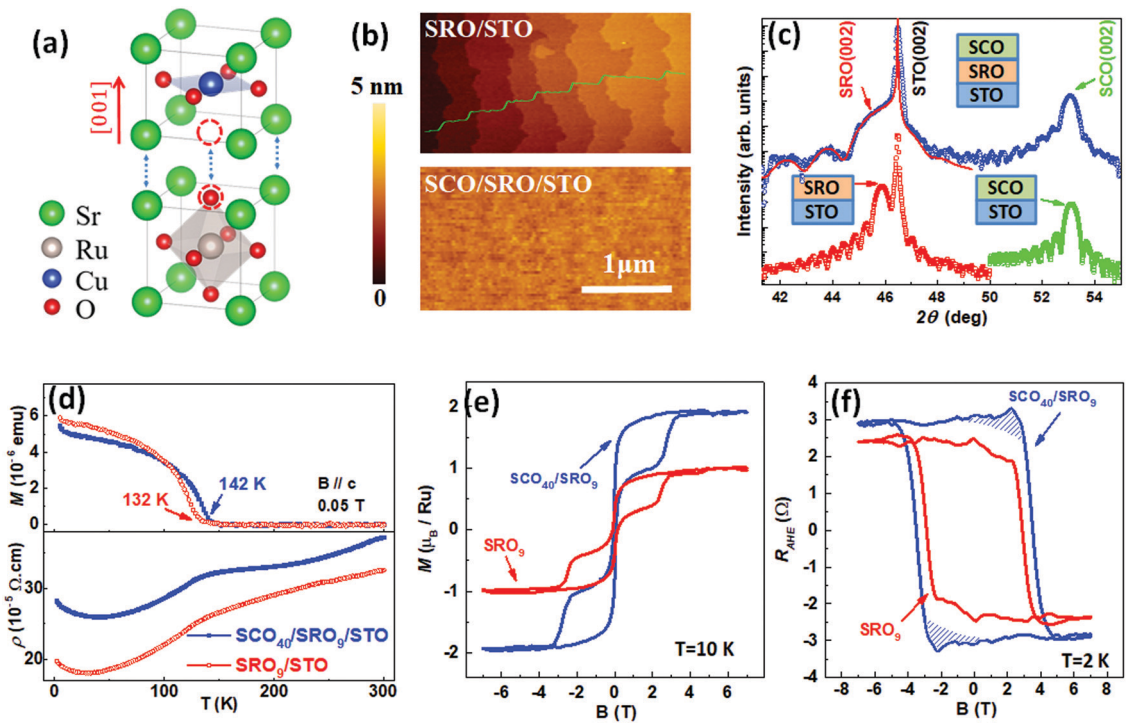

Fig. 1 (a) Schematic view for the infinite-layered SCO and perovskite SRO heterointerface. (b) Atomic force microscopy (AFM) images for the SRO_{16} bare film (top panel) and SCO_{40}/SRO_{16} bilayer film (bottom) on TiO_2-terminated STO (001) substrates. (c) θ–2θ patterns of the SRO_{25} and SCO_{40} bare films and the SCO_{40}/SRO_{16} bilayer film. The (002) peaks of SRO and SCO are marked by red and green arrows, respectively. The red line is the result of curve fitting. (d) M–T (top), and ρ–T (bottom) curves for SRO_9 bare and SCO_{40}/SRO_9 bilayer films. The M–T curves were measured under a magnetic field of 0.05 T. (e) M–H and (f) R_{AHE}–H curves for SRO_9 bare and SCO_{40}/SRO_9 bilayer films. The M–H curves were measured at 10 K. The R_{AHE}–H curves were measured at 2 K. The magnetic field was always applied along the out-of-plane direction.

preferred stacking sequence of $[CuO_2]$–[Sr]–$[RuO_2]$ at the SCO/SRO interface, implying the uniform CuO_2 plane-to-RuO_5 pyramid connections in such a heterostructure. We further found that the regularly arranged RuO_5 pyramids at the interface were elongated along the out-of-plane direction. As predicted using density-functional-theory (DFT) calculations, these features finally resulted in a high-spin state of Ru ions at the SCO/SRO interface. The elongated RuO_5 pyramids possessed an ideal electron configuration of $t_{2g}^4e_g^1$ (S = 3/2) with a highly polarized e_g orbital state, which was verified by the X-ray linear dichroism (XLD) spectra. These results demonstrate the great potential of oxygen coordination engineering in the exploration of emergent phenomena in magnetic complex oxides.

2 Results and discussion

To accurately compare the M_s, two SRO bare films were simultaneously prepared on TiO_2-terminated STO (001) substrates. Then, one SRO film was taken out for thickness calibration and magnetic measurements, and the other one was further covered with an SCO capping layer. Fig. 1(b) shows the surface morphology of a 16 unit-cell (uc) SRO_{16} film (top) and the corresponding SCO_{40}/SRO_{16} bilayer film (bottom). The bare SRO film shows a well-defined terrace structure with one-unit-cell-high steps, and the surface of the SCO/SRO bilayer film shows excellent smoothness and uniformity with a root-mean-square surface roughness of ~2.5 Å. To determine the crystal structures of SRO and SCO, the X-ray diffraction (XRD) spectra were collected for the bare and bilayer films (Fig. 1(c)). The clear thickness fringes around the (002) peak indicate the high crystallinity and good layer-by-layer epitaxial growth of the films. According to previous reports, the lattice constant of bulk SRO is 3.93 Å, larger than that of the STO substrate (3.905 Å).[31,32] Thus, the SRO layer suffered from compressive stress when deposited on (001) STO. This explains the enlarged c-axis constants that are 3.96 Å for the SRO_{25} bare film and 3.98 Å for the SCO_{40}/SRO_{16} bilayer film. For SCO, only the (002) peaks (~53.1°) are observed in the diffraction patterns. This clearly indicates that the SCO layer has a P-type structure, *i.e.*, it contains a sequence of CuO_2 planes and Sr planes stacked along the out-of-plane c-axis as shown in Fig. 1(a).[28–30]

Then, we turned our attention to the effect of the SCO capping layer on the magnetic and transport properties of SRO. Fig. 1(d)–(f) show the typical results obtained in SRO_9 and SCO_{40}/SRO_9 films. According to temperature-dependent magnetization and resistivity (M–T and ρ–T, respectively), although the bare film and the bilayer film both demonstrate itinerant ferromagnetism, where the Curie temperature (T_c) values are different. The T_c increases from 132 K to 142 K after capping with an SCO layer. The out-of-plane magnetization curve (M–H) of the SRO_9 bare film displays an M_s value of ~1.0 μ_B per f.u. at 10 K, which is consistent with the reported results.[21–23] Interestingly, the SCO_{40}/SRO_9 bilayer film shows a much larger M_s value of ~2.0 μ_B per f.u., as shown in Fig. 1(e). Considering the non-magnetic nature of SCO,[33] the enhanced M_s is exclusively attributed to the SRO layer. Another feature of the M–H curves is the magnetic phase separation in both the bare and bilayer films: a soft phase and a hard magnetic phase coexist, exhibiting obviously different coercivity fields H_c. According to Fig. 1(e), the M_s of the soft magnetic phase is significantly enhanced by capping with SCO, whereas the hard phase is less affected. We further performed Hall measurements on the two samples at 2 K. Generally, the Hall resistivity can be described as $R_{xy} = R_0\Delta B + 4\pi R_s\Delta M_s$, where the first term represents the ordinary Hall effect, and the second term represents the anomalous Hall effect (AHE) that is proportional to the film magnetization. By subtracting the linear ordinary Hall term, the R_{AHE} values of the two samples are shown in Fig. 1(f). Different from the M–H curves, there is only one phase left in the R_{AHE} curves, *i.e.*, the hard magnetic phase with the H_c increased from 2.8 T for the bare film to 3.5 T for the bilayer film. This behavior was also found by Ko *et al.* in an SRO ultrathin film with a STO capping layer.[23] Since the soft magnetic phase is invisible in the Hall measurements but produces a strongly increased magnetization, a reasonable inference is that it is an insulating phase with a high-spin state. Notably, in addition to the AHE term, the bilayer film demonstrates an anomaly as marked by the shadow areas in Fig. 1(f). This is similar to the topological Hall effect (THE) observed in ultrathin SRO films or SRO/$SrIrO_3$ multilayers.[17,36,37] The emergence of the THE in SCO/SRO bilayers can be attributed to the Dzyaloshinskii–Moriya interaction (DMI), which is due to the broken inversion symmetry at the infinite-layer/perovskite interface. This could be a topic of future work.

To prove the universality of the M_s enhancement in the bilayer structure, we changed the thickness of the SRO layer from 5 to 16 uc, while fixing the SCO capping layer to 40 uc. As shown in the M–H curves in Fig. 2(a), the existence of two magnetic phases is a common feature for all the samples. Obviously, the M_s of the SCO/SRO bilayer is always higher than that of the bare films with the same SRO thickness. The largest M_s value appears in the SCO_{40}/SRO_6 bilayer film, reaching a high-spin state of ~3.0 μ_B per f.u.. With the increase of the layer thickness of SRO, this M_s enhancement shows a gradual decline, to ~2.7 μ_B per f.u. for the SCO_{40}/SRO_7 film, to ~2.2 μ_B per f.u. for the SCO_{40}/SRO_8 film, and to ~1.1 μ_B per f.u. for the SCO_{40}/SRO_{16} film. As shown in Fig. 2(b), the M_s of the bilayer films is essentially proportional to $1/t_{SRO}$ in the range from 6 uc to 16 uc. This is the typical feature of the interfacial effect that leads to the enhancement of the magnetic moment. The only exception is for the SCO_{40}/SRO_5 film, which has a lower M_s than that of the SCO_{40}/SRO_6 film, and which could be an indication of the presence of a magnetically dead layer in the ultrathin SRO layers. The M_s value of the bare SRO film also decreases with increasing film thickness, from ~1.6–1.8 μ_B per f.u. in ultrathin films to stable values of around 1.0 μ_B per f.u. in films that are thicker than 9 uc. This trend is consistent with the recently reported results of Lu *et al.*[24] It is believed that the oxygen vacancies migrate from the STO substrate into the adjoining SRO layers during the

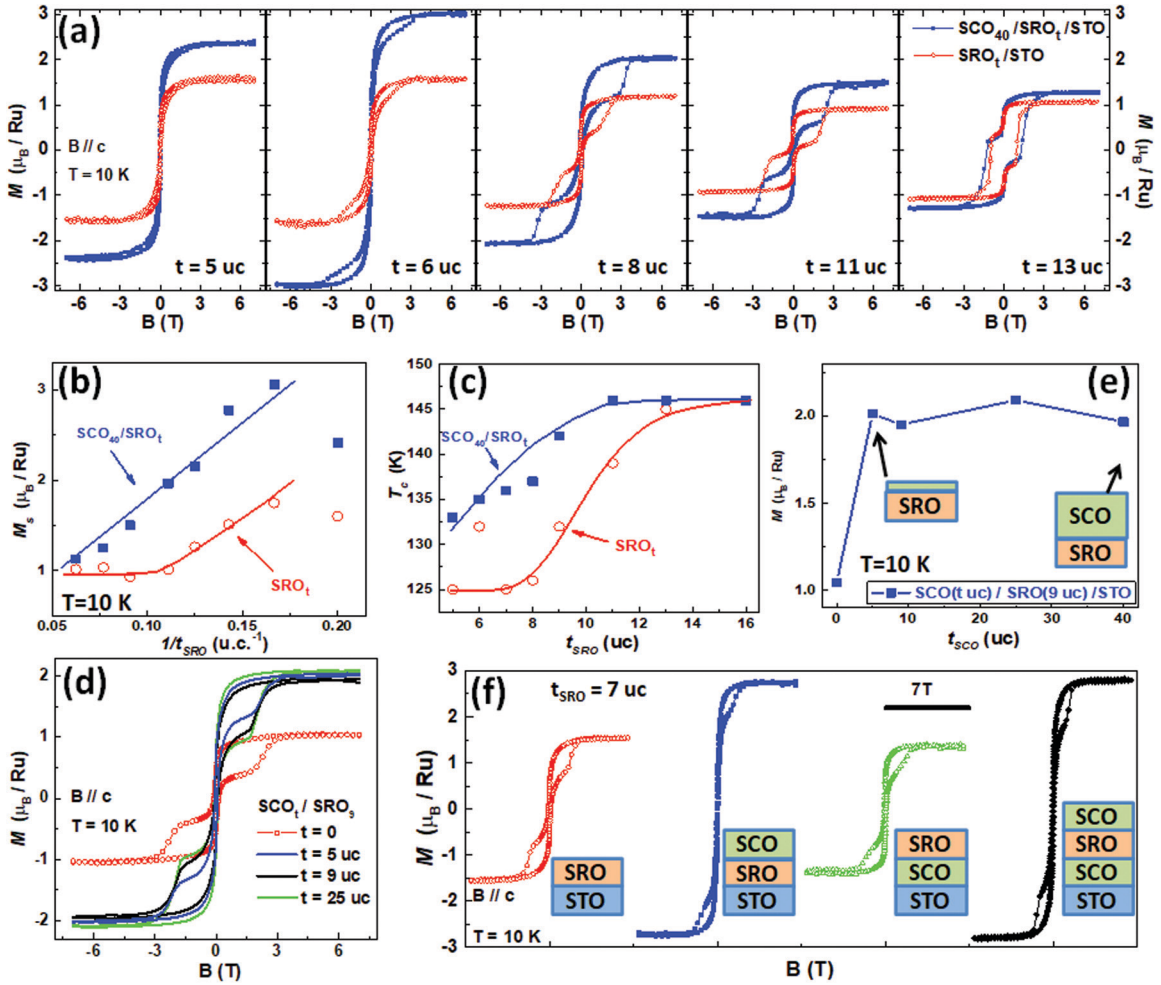

Fig. 2 (a) M–H curves for several SRO_t bare and SCO_{40}/SRO_t bilayer films with different SRO thicknesses. The M–H curves were measured under an out-of-plane magnetic field at 10 K. (b) M_s as a function of $1/t_{SRO}$ for SRO_t bare and SCO_{40}/SRO_t bilayer films with the SRO thickness ranging from 5 to 16 uc. (c) Dependence of T_c on the SRO thickness. SCO capping enhances the M_s and T_c of SRO. (d) M–H curves for SCO_t/SRO_9 films with the SCO thickness decreasing from 25 to 0 uc. The measurements were performed at 10 K under out-of-plane magnetic fields. (e) Summarized M_s of SRO_9 bare and SCO_t/SRO_9 bilayer films. (f) M–H curves for the SRO_7/STO bare film, SCO_{40}/SRO_7/STO bilayer film, SRO_7/SCO_9/STO bilayer film and $SCO_{40}/SRO_7/SCO_9$/STO trilayer film.

deposition process, leading to interfacial phases with a small H_c and a higher M_s compared with those of bulk SRO. Therefore, magnetic phase separation is observed in the bare SRO film. Fig. 2(c) shows the thickness-dependence of T_c for the bare and bilayer films. The SCO capping layer induces a remarkable increase in T_c for SRO layers that are thinner than 11 uc, with the largest increment being 12 K. And finally, the T_c value of the two sets of films rises to a consistent value of 146 K at 16 uc. Here, T_c is extracted from the M–T curves measured using an out-of-plane magnetic field of 0.05 T (see Fig. S3 in the ESI†). The higher T_c indicates the enhancement of the magnetic exchange energy in the bilayer structure, which is further confirmed by the subsequent theoretical calculations. We also investigated the thickness effect of SCO on the spin state in the bilayer structure by fixing the SRO thickness to 9 uc. As shown in Fig. 2(d) and (e), a 5 uc SCO capping layer, which is the critical thickness for the P-type structure,[34,35] is sufficient to enhance the M_s of the SRO. A further increase in SCO thickness only slightly affects the enhancement effect. Clearly, it is the nearest-neighbor P-SCO/SRO coupling that results in the abnormal high-spin state of the Ru ions.

To gain insight into the SCO/SRO interface coupling, we changed the fabrication sequence and prepared four samples on STO substrates with the same SRO_7 layer as follows: SRO_7 bare film, SCO_{40}/SRO_7 bilayer film, SRO_7/SCO_9 bilayer film and $SCO_{40}/SRO_7/SCO_9$ trilayer film. Their M–H curves are compared in Fig. 2(f). As already mentioned, the SCO_{40}/SRO_7 bilayer with an SCO/SRO interface demonstrates a significantly enhanced M_s value of $\sim$2.7 μ_B per f.u., which is almost twice that of the SRO_7 bare film ($\sim$1.5 μ_B per f.u.). Fascinatingly, the SRO_7/SCO_9 bilayer with an SRO/SCO interface is still in the normal spin state of $\sim$1.4 μ_B per f.u. Finally, the $SCO_{40}/SRO_7/SCO_9$ trilayer with both an SCO/SRO interface and an SRO/SCO interface shows a high-spin state of $\sim$2.8 μ_B per f.u., which is similar to that of the SCO_{40}/SRO_7 bilayer. This result implies that the SCO/SRO interface can enhance the M_s of SRO whereas the

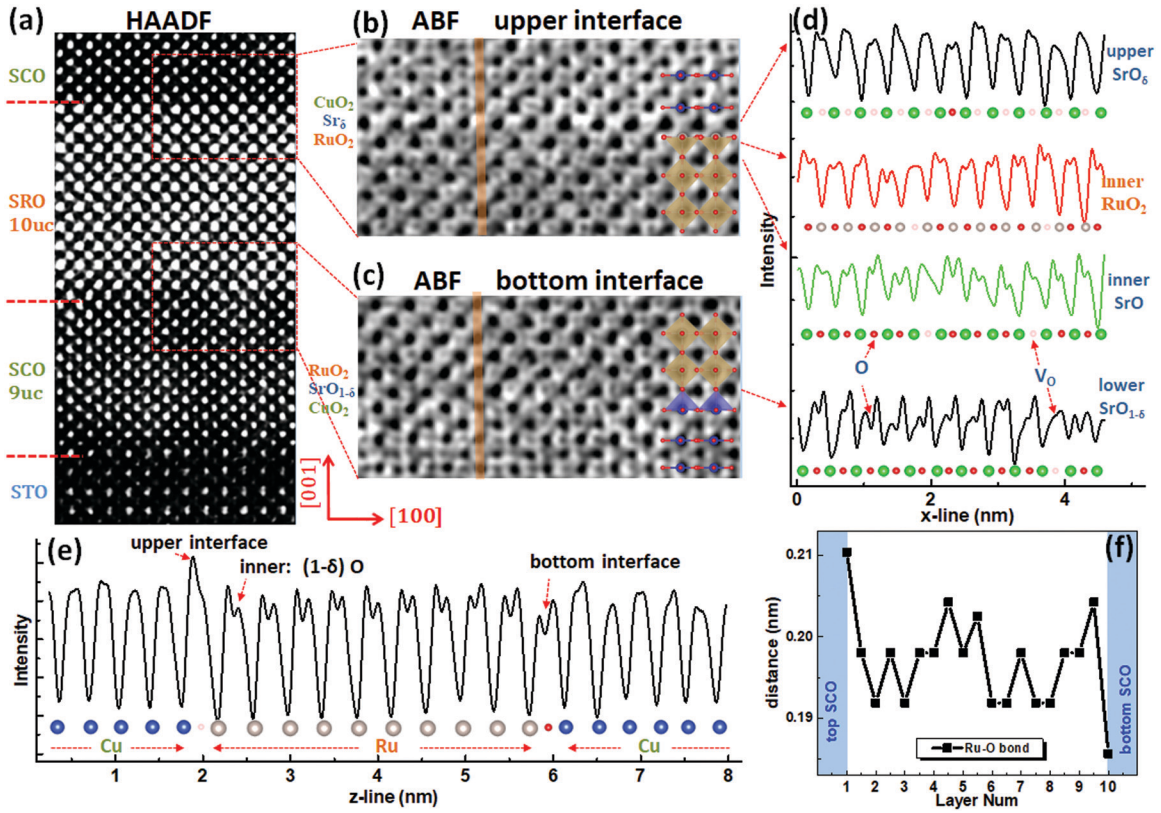

Fig. 3 (a) Typical HAADF image of the cross section of an $SCO_{40}/SRO_{10}/SCO_9$ trilayer film, recorded along the [010] zone axis. The red lines mark the SCO/SRO, SRO/SCO and SCO/STO interfaces, respectively. (b) Corresponding ABF images for the upper SCO/SRO and bottom SRO/SCO interfaces. In the schematic diagrams, the small dots represent the O ions and the larger ones represent the Cu/Ru ions. (d) Horizontal line profiles of the ABF images at the upper interfacial SrO_δ plane, inner RuO_2 plane, inner SrO plane and bottom interfacial $SrO_{1-\delta}$ plane. The green, gray, blue and red dots represent the Sr, Ru, Cu and O sites, respectively. The red hollows represent the oxygen vacancies (V_o). (e) Vertical line profile by averaging 10 line profiles along the Cu/Ru columns. The absence or presence of O ions at the upper or bottom interface is clearly demonstrated. (f) The different Ru–O bond distances in the SRO layers from the top interface to the bottom interface. Significant elongation of the Ru–O bond distance at the top SCO/SRO interface is identified.

inverted SRO/SCO interface cannot. Generally, the bottom 9 uc SCO is thick enough to form the P-type structure. So, this difference needs to be understood based on microscopic information.

Fig. 3(a) presents the high-angle annular dark-field (HAADF) image of the cross-section of an $SCO_{40}/SRO_{10}/SCO_9$ trilayer film, recorded using high-resolution scanning transmission electron microscopy (STEM) along the [010] zone axis. According to the different brightness of the heavier cations, three distinct interfaces can be identified from top to bottom. The brightest dots correspond to Ru. Sr is dimmer than Ru but brighter than Cu, and Ti is the dimmest. All the interfaces are very sharp, indicating the high-quality epitaxial growth of the multilayers without visible cation intermixing. To determine the O ions, the annular bright-field (ABF) image was acquired simultaneously for the same region. The lattice images of the upper SCO/SRO interface and the bottom SRO/SCO interface are magnified in Fig. 3(b) and (c). In the ABF image, the small dark dot between the large cation dots represents the O site. It becomes faded or even whitened when the oxygen vacancy occurs. As expected, the SRO is a virtually perovskite structure and the SCO is an infinite-layered structure. However, the interfaces show a very complex structure. At first glance, there is a substantial number of oxygen vacancies in the upper SCO/SRO interface, forming a preferred stacking sequence of $[CuO_2]$–[Sr]–$[RuO_2]$ along the *c*-axis. By contrast, the bottom SRO/SCO interface has very few oxygen vacancies, suggesting a preferred stacking sequence of $[RuO_2]$–[SrO]–$[CuO_2]$. The horizontal intensity profiles taken around the upper and bottom interfaces show this distinction more explicitly (Fig. 3(d)). There are two kinds of valleys that occur in the ABF line profiles: the deep ones represent A- or B-site cations and the shallow ones represent the O sites. In the upper interface, the oxygen valleys are weakened or clearly disappear, implying the formation of an SrO_δ layer. By contrast, the oxygen valleys are still apparent at the bottom interface with very few vacancy (V_o) sites, implying an $SrO_{1-\delta}$ layer. These results allow us to figure out the microscopic interface structure (schematic diagrams in Fig. 3(b) and (c)). The upper SCO/SRO interface is formed by CuO_2-plane-to-RuO_5-pyramid connections that possibly support a high-spin state of Ru. By contrast, the bottom SRO/SCO interface is formed by RuO_6-octahedra-to-CuO_5-pyramid connections that do not change the Ru moment. Moreover, the line profiles of the inner RuO_2 and SrO planes

indicate that the SCO capping layer will introduce more oxygen vacancies that are ~2–3 uc SRO below the upper interface, which will also support the high-spin state of Ru.

Fig. 3(e) shows the vertical intensity profile along Cu/Ru sites as a function of the atomic position, obtained by averaging 10 sets of *z*-line profile data. The absence of O ions in upper interfacial Sr plane and the slight O-deficiency for the inner layers are plainly confirmed by these statistical data. These results reveal the importance of termination control in the growth of ABO_2/ABO_3 heterojunctions. Since the multilayer is deposited on the TiO_2-terminated STO (001) substrate, the termination layer of bottom SCO should be the $[CuO_2]$ plane. When further depositing the SRO layer, the next layer prefers an [SrO] plane. By contrast, for the upper SCO/SRO interface with an $[RuO_2]$ terminated layer, the subsequent deposition of SCO naturally prefers an [Sr] plane. The latter leads to the unique RuO_5 pyramid-structure at the upper SCO/SRO interface.

To gain more information on the interface coupling effect, Fig. 3(f) shows the bond distances between Ru and O ions along the *z* direction (extracted from the line profile in Fig. 3(e)). Surprisingly, the Ru–O bond distance in the interfacial RuO_5 pyramid is ~2.10 Å, which is notably larger than the average value of 1.98 Å obtained in the inner layers far away from the interface. This indicates that the well-ordered RuO_5 pyramids at the SCO/SRO interface are significantly elongated along the *c*-axis. This distortion of the RuO_5 pyramids will lower the orbitals of 4d electrons in the *z* direction and then stabilize the high-spin state of Ru, as will be discussed later. By contrast, the Ru–O bond distance is reduced to 1.86 Å at the bottom SRO/SCO interface, which is against the orbital occupancy in the *z* direction.

To obtain knowledge about the interfacial electronic structure, we constructed the SCO_4/SRO_5 heterostructure with a $[CuO_2]$–[Sr]–$[RuO_2]$ interface and performed DFT calculations. After lattice relaxation and self-consistent calculations, we find that the Ru–O bond at the interface is indeed elongated along the *z* direction: it is ~2.05 Å in the RuO_5 pyramids and ~1.96 Å in the inner RuO_6 octahedra, exhibiting the same trend as with the STEM results. More importantly, as shown in Fig. 4(a) and Fig. S4(b) (see in the ESI†), the density of states (DOS) of the SRO layers show substantial spin and orbital reconstructions of the Ru 4d and O 2p states near the interface. For the Ru ions,

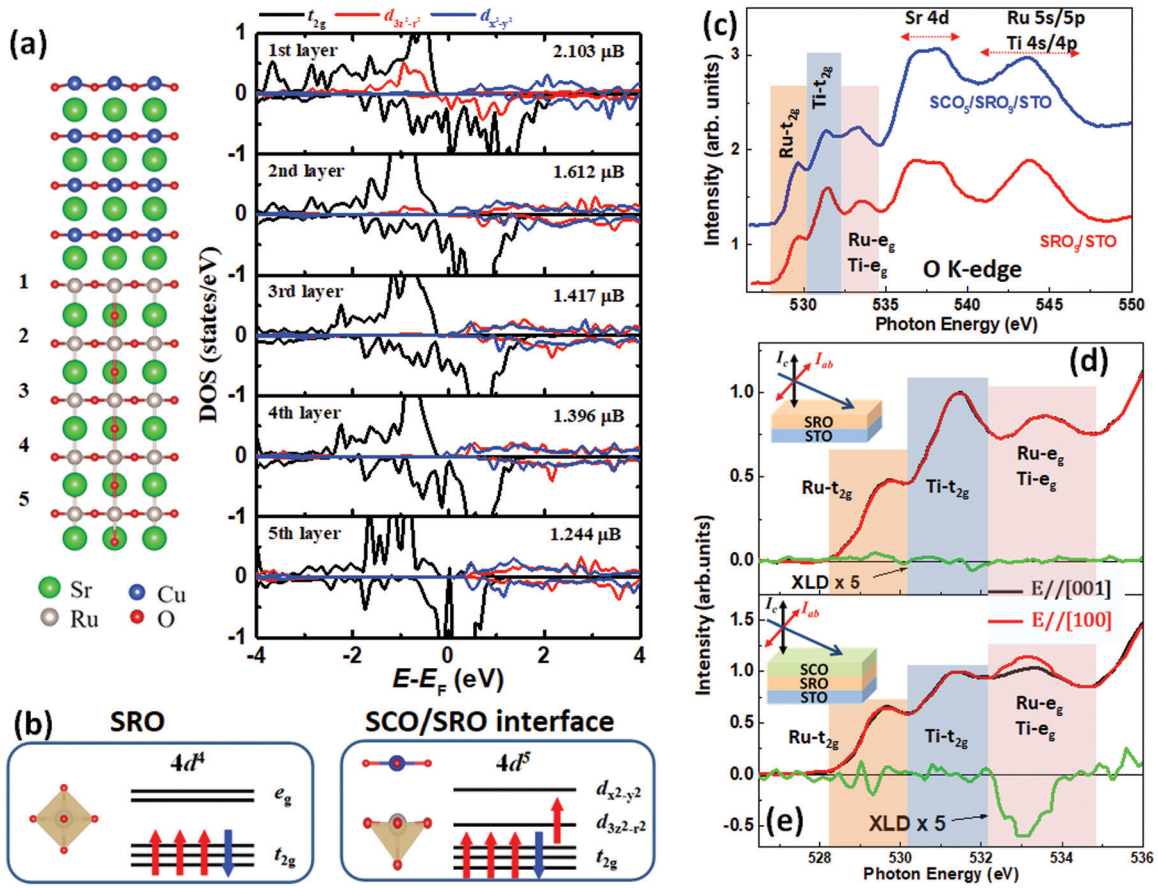

Fig. 4 (a) Left: Structural model of the $[CuO_2]$–[Sr]–$[RuO_2]$-type interface for DFT calculations in which the green, gray, blue and red dots represent the Sr, Ru, Cu and O ions, respectively. Right: Resulting DFT layer-dependent DOS of Ru 4d states in five adjacent layers near the interface. (b) Schematics of electron configurations for low-spin Ru^{4+} in the RuO_6 octahedron (left) and high-spin Ru^{5+} in the RuO_5 pyramid (right). (c) Normalized XAS spectra of the O K-edge for the SRO_9 bare and SCO_5/SRO_9 bilayer films. (d and e) Normalized XLD spectra of the O K-edge for the SRO_9 bare film (d), and the SCO_5/SRO_9 bilayer film (e), measured using a linear X-ray beam with different polarizations (see in Experimental section). The deduced XLD spectrum ($I_c - I_{ab}$) is given by the green line. The XLD peak value of the SCO_5/SRO_9 bilayer film is as large as −11%.

the $d_{3z^2-r^2}$ state is obviously formed below the Fermi level in the 1st and 2nd SRO layers, implying the electron occupancy of the e_g orbitals. This is because, in the $[CuO_2]$–[Sr]–$[RuO_2]$-type interface, the depletion of apical oxygen will provide extra electrons to the interface. The elongation of RuO_5 pyramids along the *z* direction further changes the crystal-field splitting, which finally results in a stable high-spin state with an electron configuration of $t_{2g}^4e_g^1$ (S = 3/2). Differently, the DOS of the SRO layers far away from the interface (3rd, 4th and 5th layers) are similar to those of bulk SRO. The electrons occupy the t_{2g} bands, forming a t_{2g}^4 electron configuration with the low-spin state (S = 1). The calculated spin moments on the Ru sites are $\sim$2.1 μ_B in the 1st layer and $\sim$1.6 μ_B in the 2nd layer, both of which are higher than the $\sim$1.4 μ_B of the SRO bulk. Considering that SRO is an itinerant ferromagnet with delocalized 4d orbitals strongly hybridized with O 2p orbitals, the O sites will also contribute to the M_s, as confirmed by XMCD measurements or DFT calculations.[15,16] Fig. S4(b) (ESI†) summarizes the DOS on the Ru, O and Sr sites for the five SRO layers. We find that the O 2p states demonstrate a larger spin polarization near the interface region, leading to the effective M_s values of $\sim$0.66 μ_B in the 1st layer and $\sim$0.50 μ_B in the 2nd layer. Thus, the total M_s demonstrates a maximum value of $\sim$2.8 μ_B per SRO formula unit in the 1st layer, which is gradually reduced to $\sim$1.8 μ_B in the 5th layer, in good agreement with the magnetic measurements. Based on these results, the schematic electronic configurations for the low-spin Ru^{4+} in bulk SRO and the high-spin Ru^{3+} at the SCO/SRO interface are shown in Fig. 4(b). Different from the discrete RuO_5 structure induced by random oxygen vacancies, the regularly arranged RuO_5 pyramids at the interface present a *z*-elongation, which lowers the e_g orbital not only in itself but also in the adjacent SRO layer. This indicates that the charge and orbital reconstruction are essential for the rare high-spin state SRO at the $[CuO_2]$–[Sr]–$[RuO_2]$ interface. We also calculate the magnetic exchange energy for the SRO layer with or without an SCO capping layer. Indeed, the interfacial RuO_5 pyramid layer in the SCO/SRO heterostructure has an exchange energy larger than that of the SRO bare film (37.8 meV *versus* 36.8 meV). This indicates that the structure reconstruction at the SCO/SRO interface is responsible for the increase in T_c. As revealed by the DOS, the coupling effect in the SCO/SRO heterostructure leads to considerable occupancy of the e_g orbitals for the interfacial SRO layers. It is possible that the occupied e_g electrons induce additional exchange interactions between the Ru ions, thus enhancing the T_c.

To experimentally check the band structure, we performed O K-edge XAS and XLD studies on the SRO_9/STO bare film and the SCO_5/SRO_9/STO bilayer film. Generally, the O K-edge peak stems from excitation from the O 1s core level to the unoccupied O 2p orbitals. The latter are strongly hybridized with the d orbitals of the transition metal oxides near the Fermi level. In particular, the t_{2g} and e_g metal orbitals have π overlap and σ overlap with the O 2p states, respectively. Thus, the intensity of the O K-edge peaks can reflect the number of empty d states. Indeed, it has already been used to determine information on the unoccupied states of Ru 4d orbitals.[38–40] As shown in Fig. 4(c), there are five resonance features identified around the O K-edge. According to the references, the peak from 528.2 to 530.2 eV is associated with the hybridization with Ru t_{2g} orbitals. The peak from 530.4 to 531.8 eV should be related to hybridization with Ti t_{2g} orbitals since it is absent in the case with thicker SRO layers as shown in Fig. S5 (see in the ESI†). The broader resonance at higher photon energies, from 532.2 to 534.8 eV, can be explained by the combined contribution of Ru e_g and Ti e_g states.[38] Considering that the peak of the Ti e_g orbitals is usually wide with a relatively low intensity, the contribution of the Ru e_g states is more significant here.[41,42] Finally, the structures from 535 to 549 eV are derived from the O 2p orbitals mixed with the Sr 4d, Ru 5s/5p and Ti 4s/4p states.

Based on the above analysis, the O K-edge XLD spectra around the d-orbital-derived region are obtained by two X-ray polarizations with a fixed incident angle of 70° to the film normal. Here, the spectra are normalized using the intensity of the Ti t_{2g}-associated peak. The absorption signal I_{ab} with X-ray polarization parallel to [100] or [010] reflects the O $2p_x$ and $2p_y$ characteristics hybridized with the Ru d_{xy} and $d_{x^2-y^2}$ states. The signal I_c with X-ray polarization nearly parallel to [001] reflects the O $2p_z$ characteristic hybridized with the Ru d_{xz}, d_{yz} and $d_{3z^2-r^2}$ states. The XLD signals ($I_c - I_{ab}$) thus give measurements of the different occupancies of the Ru 4d orbitals. As shown in Fig. 4(d) and (e), the most significant difference between the bare and bilayer films appears around the e_g states. Negligible signals are observed in the SRO/STO bare film. This is reasonable since both the Ru^{4+} and Ti^{4+} ions have the empty e_g bands. After SCO capping, the Ru^{3+} ions in the RuO_5 pyramids have an electron configuration of $t_{2g}^4e_g^1$ ($4\uparrow,1\downarrow$) that favors the $d_{3z^2-r^2}$ occupancy as predicted by DFT calculations. This is well proved by the large orbital polarization of the $d_{3z^2-r^2}$ states (−11%,) identified in the SCO/SRO/STO bilayer film. The XLD of the Ru t_{2g} states also becomes slightly visible in the bilayer structure. This is possibly because the d_{xz}, d_{yz} and d_{xy} orbitals are degenerate in the elongated RuO_5 pyramids.

3 Conclusion

In summary, a rare high-spin state of the SRO film, as large as $\sim$3.0 μ_B per f.u., is achieved by capping a P-type infinite-layered SCO film. This enhancement of M_s gradually declines with the thickness of the SRO film, indicating that it originates from the interface effect in the SCO/SRO heterostructure. The atomic-scale lattice images clearly demonstrate the preferred stacking sequence of $[CuO_2]$–[Sr]–$[RuO_2]$ at the SCO/SRO interface, which forms the well-ordered CuO_2-plane-to-RuO_5-pyramid connections. The regularly arranged RuO_5 pyramids are further elongated along the *c*-axis by the coupling effect with SCO, finally supporting a stable high-spin state with an electron configuration of $t_{2g}^4e_g^1$ as predicted *via* DFT calculations. The increase in T_c by the SCO capping is identified in the *M*–*T* curves, which can be explained by the enhanced magnetic exchange energy in the SCO/SRO heterostructure. The unique band structure further causes a large orbital polarization of the

Ru e_g state, which is well proved *via* the XLD spectra. Our results demonstrate that oxygen coordination engineering at the infinite-layer/perovskite oxide interface is a promising approach for creating well-ordered oxide pyramid-structures with unique orbital configurations and associated characteristics, opening avenues towards advanced oxide electronics.

4 Experimental section

Thin film growth

High-quality $SrCuO_2/SrRuO_3$ bilayer films were epitaxially grown on atomically flat TiO_2-terminated $SrTiO_3$(001) substrates (Fig. S1, ESI†) using the technique of pulsed laser deposition (KrF, λ = 248 nm). The SRO and SCO bare films were also prepared for comparison. The growth of SRO layers was conducted at 670 °C under an oxygen pressure of 20 Pa with a laser fluence of 2.5 J cm^{-2}. The growth of SCO layers was conducted at 620 °C under an oxygen pressure of 20 Pa with a laser fluence of 1.8 J cm^{-2}. After deposition, the sample was allowed to cool naturally to room temperature in the furnace under an oxygen pressure of 100 Pa. The film thickness was determined *via* deposition time. The deposition rates for the SRO layer and the SCO layer were carefully calibrated using the technique of small angle X-ray reflectivity (XRR, see Fig. S2, ESI†). Following this procedure, trilayer samples of $SrCuO_2/SrRuO_3/SrCuO_2$ on the $SrTiO_3$(001) surface were also prepared for STEM measurements.

Sample characterization

The surface morphology of the as-prepared films was measured using atomic force microscopy (AFM, SPI 3800N, Seiko). The crystal structure was determined using a high-resolution X-ray diffractometer (D8 Discover, Bruker) with Cu-Kα radiation. The magnetic properties were measured using a quantum design vibrating sample magnetometer (VSM-SQUID) at the temperature range of 5–300 K. The magnetic field was applied along the out-of-plane direction of the (001) films. Transport measurements were performed using a quantum design physical property measurement system (PPMS) with an applied current of 10 μA with standard Hall bar geometry. Atomic-scale lattice images were recorded by high-resolution scanning transmission electron microscopy (STEM), with double C_S correctors (JEOL-ARM200F). To detect the oxygen vacancies in the SRO layers, the annular bright-field (ABF) imaging mode was employed along with the high-angle annular dark-field (HAADF) imaging mode. Cross-sectional thin samples for STEM analysis were prepared using a dual-beam focused ion beam system along the [010] direction.

X-Ray absorption spectroscopy

The XAS measurements were performed using the BL08U1A beamline at the Shanghai Synchrotron Radiation Facility at room temperature in a total electron yield mode. As shown in the insets of Fig. 4(d) and (e), the XLD spectra of the oxygen K edge were measured for the two polarization directions of the linearly polarized X-ray with an incident angle of 70° to the film normal. E is the electric field of the X-ray. I_{ab} (E//[100] or [010]) and I_c (E//[001]) are the absorption intensities that correspond to the in-plane direction and the out-of-plane direction, respectively. The measurement temperature was 300 K.

Density functional theory calculations

DFT calculations were performed using the Vienna *ab initio* simulation package (VASP) codes,[43] with the generalized gradient approximation of Perdew–Burke–Ernzerhof modified for solids (PBEsol),[44,45] the exchange correlation functional and the projector augmented wave (PAW)[46] pseudopotentials. The Monkhorst–Pack k-mesh[47] of 13 × 13 × 1 over the Brillouin zone with a cutoff energy of 600 eV for the plane waves was found to yield convergence of all the properties computed. The correlation effects on Ru and Cu were treated within the DFT+U approach using the formalism of Dudarev.[48] Values of U = 2.5 eV and J = 0.4 eV were applied on the Ru 4d orbitals[49] and values of U = 7.5 eV and J = 0.98 eV were adopted for the Cu 3d orbitals.[50] The in-plane lattice constants were fixed to 5.52 Å, which is the experimental lattice constant ($\sqrt{2}a$) of $SrTiO_3$. All ions were free to move until the Hellmann–Feynman force on each atom was smaller than 0.01 eV $Å^{-1}$ and the absolute total energy difference between the two successive loops was less than 10^{-5} eV.

Conflicts of interest

There are no conflicts to declare.

Acknowledgements

We gratefully acknowledge the discussion on sample fabrication with Professor Lingfei Wang in Hefei National Laboratory for Physical Sciences at Microscale, University of Science and Technology of China. This work is supported by the Science Center of the National Science Foundation of China (Grant No. 52088101), the National Basic Research of China (Grants No. 2018YFA0305704, No. 2017YFA0206300, No. 2017YFA0303601, and No. 2019YFA0704904), the Project for Innovative Research Team of the National Natural Science Foundation of China (Project No. 11921004), the National Natural Science Foundation of China (Grants No. 11934016 and No. 51972335), the Strategic Priority Research Program (B) of the Chinese Academy of Sciences (No. XDB33030200), and the Key Program of the Chinese Academy of Sciences. We acknowledge Beamline BL08U1A at the Shanghai Synchrotron Radiation Facility (SSRF) for the XAS characterizations.

References

1 A. Umezawa, W. Zhang, A. Gurevich, Y. Feng, E. Hellstrom and D. Larbalestier, *Nature*, 1993, **364**, 129.
2 J.-H. Park, E. Vescovo, H.-J. Kim, C. Kwon, R. Ramesh and T. Venkatesan, *Nature*, 1998, **392**, 794.
3 Y. Tokura and N. Nagaosa, *Science*, 2000, **288**, 462.

4 M. Imada, A. Fujimori and Y. Tokura, *Rev. Mod. Phys.*, 1998, **70**, 1039.
5 J. M. De Teresa, A. Barthelemy, A. Fert, J. P. Contour, F. Montaigne and P. Seneor, *Science*, 1999, **286**, 507.
6 Y. Tokura, Y. Taguchi, Y. Okada, Y. Fujishima, T. Arima, K. Kumagai and Y. Iye, *Phys. Rev. Lett.*, 1993, **70**, 2126.
7 F. Trier, G. E. Prawiroatmodjo, Z. Zhong, D. V. Christensen, M. von Soosten, A. Bhowmik, J. M. G. Lastra, Y. Chen, T. S. Jespersen and N. Pryds, *Phys. Rev. Lett.*, 2016, **117**, 096804.
8 S. Okamoto and A. J. Millis, *Nature*, 2004, **428**, 630.
9 J. Mannhart and D. G. Schlom, *Science*, 2010, **327**, 1607.
10 A. Callaghan, C. W. Moeller and R. Ward, *Inorg. Chem.*, 1966, **5**, 1572.
11 J. Longo, P. Raccah and J. Goodenough, *J. Appl. Phys.*, 1968, **39**, 1327.
12 R. Bouchard and J. Gillson, *Mater. Res. Bull.*, 1972, **7**, 873.
13 C. Jones, P. Battle, P. Lightfoot and W. Harrison, *Acta Crystallogr., Sect. C: Cryst. Struct. Commun.*, 1989, **45**, 365.
14 I. Mazin and D. J. Singh, *Phys. Rev. B: Condens. Matter Mater. Phys.*, 1997, **56**, 2556.
15 A. Grutter, F. Wong, E. Arenholz, A. Vailionis and Y. Suzuki, *Phys. Rev. B: Condens. Matter Mater. Phys.*, 2012, **85**, 134429.
16 S. Thomas, B. Kuiper, J. Hu, J. Smit, Z. Liao, Z. Zhong, G. Rijnders, A. Vailionis, R. Wu and G. Koster, *Phys. Rev. Lett.*, 2017, **119**, 177203.
17 Y. Ohuchi, J. Matsuno, N. Ogawa, Y. Kozuka, M. Uchida, Y. Tokura and M. Kawasaki, *Nat. Commun.*, 2018, **9**, 1.
18 M. Ye, S. Hu, Y. Zhu, Y. Zhang, S. Ke, L. Xie, Y. Zhang, S. Hu, D. Zhang and Z. Luo, *Nano Lett.*, 2020, **21**, 144.
19 M. Laad and E. Müller-Hartmann, *Phys. Rev. Lett.*, 2001, **87**, 246402.
20 P. Allen, H. Berger, O. Chauvet, L. Forro, T. Jarlborg, A. Junod, B. Revaz and G. Santi, *Phys. Rev. B: Condens. Matter Mater. Phys.*, 1996, **53**, 4393.
21 P. A. Kumar, P. Joy and S. Date, *Physica B*, 1999, **269**, 356.
22 S. Bushmeleva, V. Y. Pomjakushin, E. Pomjakushina, D. Sheptyakov and A. Balagurov, *J. Magn. Magn. Mater.*, 2006, **305**, 491.
23 E. K. Ko, J. Mun, H. G. Lee, J. Kim, J. Song, S. H. Chang, T. H. Kim, S. B. Chung, M. Kim and L. Wang, *Adv. Funct. Mater.*, 2020, **30**, 2001486.
24 J. Lu, L. Si, X. Yao, C. Tian, J. Wang, Q. Zhang, Z. Lai, I. A. Malik, X. Liu and P. Jiang, *Phys. Rev. B*, 2020, **101**, 214401.
25 J. Lu, L. Si, Q. Zhang, C. Tian, X. Liu, C. Song, S. Dong, J. Wang, S. Cheng and L. Qu, *Adv. Mater.*, 2021, 2102525.
26 I. Solodov, J. Wackerl, K. Pfleiderer and G. Busse, *Appl. Phys. Lett.*, 2004, **84**, 5386.
27 D. Norton, B. Chakoumakos, J. Budai, D. Lowndes, B. Sales, J. Thompson and D. Christen, *Science*, 1994, **265**, 2074.
28 D. Di Castro, C. Cantoni, F. Ridolfi, C. Aruta, A. Tebano, N. Yang and G. Balestrino, *Phys. Rev. Lett.*, 2015, **115**, 147001.
29 Z. Liao, E. Skoropata, J. Freeland, E.-J. Guo, R. Desautels, X. Gao, C. Sohn, A. Rastogi, T. Z. Ward and T. Zou, *Nat. Commun.*, 2019, **10**, 1.
30 S. Li, Q. Zhang, S. Lin, X. Sang, R. F. Need, M. A. Roldan, W. Cui, Z. Hu, Q. Jin and S. Chen, *Adv. Mater.*, 2021, **33**, 2001324.
31 C.-B. Eom, R. Cava, R. Fleming, J. M. Phillips, J. Marshall, J. Hsu, J. Krajewski and W. Peck, *Science*, 1992, **258**, 1766.
32 Q. Gan, R. Rao, C. Eom, J. Garrett and M. Lee, *Appl. Phys. Lett.*, 1998, **72**, 978.
33 T. Siegrist, S. Zahurak, D. Murphy and R. Roth, *Nature*, 1988, **334**, 231.
34 Z. Zhong, G. Koster and P. J. Kelly, *Phys. Rev. B: Condens. Matter Mater. Phys.*, 2012, **85**, 121411.
35 M. Dantz, J. Pelliciari, D. Samal, V. Bisogni, Y. Huang, P. Olalde-Velasco, V. N. Strocov, G. Koster and T. Schmitt, *Sci. Rep.*, 2016, **6**, 32896.
36 Q. Qin, L. Liu, W. N. Lin, X. Y. Shu, Q. D. Xie, Z. h. Lim, C. J. Li, S. K. He, G. M. Chow and J. S. Chen, *Adv. Mater.*, 2019, **31**, 1807008.
37 C. Wang, C. H. Chang, A. Herklotz, C. Chen, F. Ganss, U. Kentsch, D. Chen, X. S. Gao, Y. J. Zeng, O. Hellwig, M. Helm, S. Gemming, Y. H. Chu and S. Q. Zhou, *Adv. Electron. Mater.*, 2020, **6**, 2000184.
38 M. Schmidt, T. Cummins, M. Bürk, D. Lu, N. Nücker, S. Schuppler and F. Lichtenberg, *Phys. Rev. B: Condens. Matter Mater. Phys.*, 1996, **53**, R14761.
39 T. Mizokawa, L. Tjeng, G. Sawatzky, G. Ghiringhelli, O. Tjernberg, N. Brookes, H. Fukazawa, S. Nakatsuji and Y. Maeno, *Phys. Rev. Lett.*, 2001, **87**, 077202.
40 M. Malvestuto, E. Carleschi, R. Fittipaldi, E. Gorelov, E. Pavarini, M. Cuoco, Y. Maeno, F. Parmigiani and A. Vecchione, *Phys. Rev. B: Condens. Matter Mater. Phys.*, 2011, **83**, 165121.
41 M. Abbate, J. Guevara, S. Cuffini, Y. Mascarenhas and E. Morikawa, *Eur. Phys. J. B*, 2002, **25**, 203.
42 F. Frati, M. O. Hunault and F. M. de Groot, *Chem. Rev.*, 2020, **120**, 4056.
43 G. Kresse and J. Furthmüller, *Phys. Rev. B: Condens. Matter Mater. Phys.*, 1996, **54**, 11169.
44 J. P. Perdew, K. Burke and M. Ernzerhof, *Phys. Rev. Lett.*, 1996, **77**, 3865.
45 J. P. Perdew, A. Ruzsinszky, G. I. Csonka, O. A. Vydrov, G. E. Scuseria, L. A. Constantin, X. Zhou and K. Burke, *Phys. Rev. Lett.*, 2008, **100**, 136406.
46 G. Kresse and D. Joubert, *Phys. Rev. B: Condens. Matter Mater. Phys.*, 1999, **59**, 1758.
47 H. J. Monkhorst and J. D. Pack, *Phys. Rev. B: Solid State*, 1976, **13**, 5188.
48 S. L. Dudarev, G. A. Botton, S. Y. Savrasov, C. J. Humphreys and A. P. Sutton, *Phys. Rev. B: Condens. Matter Mater. Phys.*, 1998, **57**, 1505.
49 K. Gupta, B. Mandal and P. Mahadevan, *Phys. Rev. B: Condens. Matter Mater. Phys.*, 2014, **90**, 125109.
50 V. I. Anisimov, J. Zaanen and O. K. Andersen, *Phys. Rev. B: Condens. Matter Mater. Phys.*, 1991, **44**, 943.

